2026 IEEE International Conference on Robotics and Automation (ICRA 2026)
June 1-5, 2026. Vienna, Austria

MorphoBall: A Bio-Inspired Transformable Spherical Robot with Dual Terrestrial Gaits and Surface Swimming Capability

Jinyuan Liu[1], Guangzhi Tian[2], Yuqiang Jin[1], Ling Shi[2], Minglei Fu[1], Wenan Zhang[1] and Bo Chen[1]

Abstract— **MorphoBall is a bio-inspired, deformable spherical robot designed for multimodal locomotion across terrestrial and aquatic environments. By integrating a dual-mode drive system (spherical rolling and differential-drive) with a morphology-mediated propulsion mechanism, MorphoBall achieves adaptive mobility in diverse terrains, including flat ground, slopes, and water surfaces. A key innovation lies in the dual-function ciliary band, which provides both passive damping during terrestrial rolling and active propulsion during aquatic navigation. Model-based controllers are developed to regulate forward velocity, trajectory curvature, and roll tilt angle, demonstrating superior stability and responsiveness compared to baseline PID implementations. Experimental results validate MorphoBall's ability to autonomously navigate structured indoor environments and traverse unstructured outdoor terrains, achieving seamless mode transitions and completing missions 34% faster than single-morphology strategies. This work highlights the potential of morphology adaptation as a tool for enhancing environmental adaptability in mobile robotics.**

I. Introduction

Mobile robots are increasingly deployed in challenging environments such as disaster zones, wetlands, and extraterrestrial terrains, where adaptability to diverse conditions is critical for mission success [1]–[3]. Among various robotic platforms, spherical robots stand out for their fully enclosed design [4], [5], which provides inherent robustness against environmental hazards, including water ingress, debris impact, and rough terrain traversal. This structural advantage enables seamless transitions between land and water while maintaining mechanical integrity and operational reliability. However, despite these benefits, existing spherical robots often face limitations in propulsion efficiency [6], locomotion versatility, and adaptability to complex terrains, hindering their widespread adoption in real-world applications.

Spherical robots have been extensively studied for their robustness and simplicity in motion control. For instance, [7], [8] and [9] achieve terrestrial locomotion through pure rolling, while [10]–[12] enhances maneuverability by employing a car-driven spherical robot with an internal actuation mechanism. However, these designs primarily focus on single-mode operation, limiting their adaptability to complex terrains such as slopes or narrow gaps. To address multimodal and all-terrain mobility, researchers have proposed various solutions. [13] introduced a robot capable of switching between 'rolling mode' and 'obstacle-crossing mode' via a reconfigurable linkage mechanism. [14] designed a robot with a soft inflatable shell to adapt to diverse terrains, while [15] developed a dual-mode spherical robot that combines pendulum-based rolling with spring-assisted jumping to enhance terrain adaptability in deep-space exploration scenarios. Despite their demonstrated adaptability, these approaches often introduce additional structural components, leading to increased energy consumption, higher system complexity, and greater challenges in control and modeling.

On the other hand, amphibious robots [16], [17] typically integrate separate terrestrial and aquatic propulsion mechanisms, resulting in increased structural complexity and energy consumption [18], [19]. Although recent advances in deformable structures [20] have shown potential for enhancing mobility, their applications remain largely confined to terrestrial scenarios. Moreover, while the vast majority of spherical robots rely on passive buoyancy to achieve surface swimming [21], their propulsion performance is inherently limited due to their smooth surfaces. This limitation becomes particularly critical when operating in cluttered water environments, as the lack of active propulsion mechanisms may lead to a loss of mobility if obstructed by debris.

These limitations highlight a significant research gap: the need for a unified platform that combines multimodal terrestrial locomotion, efficient aquatic propulsion, and reliable morphological adaptation without increasing system complexity. Bridging this gap could unlock new possibilities for mobile robotics in dynamic and heterogeneous environments. In this work, we introduce MorphoBall, a bio-inspired, deformable spherical robot engineered to meet this challenge. The key contributions of this work are as follows:

(i) A unified drive system that integrates spherical rolling and differential-drive modes, enabling adaptive mobility on flat ground, slopes, and narrow passages.
(ii) A dual-function ciliary band that limits roll tilt angles and assists in steering during terrestrial rolling, while enhancing propulsion through increased viscous drag during aquatic navigation, thereby eliminating the need for additional actuators or external mechanisms.
(iii) A hierarchical control architecture that achieves precise regulation of forward velocity, trajectory curvature, and roll tilt angle, validated through extensive experiments in both structured indoor and unstructured outdoor environments.

This work was supported by the National Key Research and Development Program of China under Grant 2025YFE0113300, and the Key R&D Program of Zhejiang Province under Grant 2026C04033.

[1]Jinyuan Liu, Yuqiang Jin, Minglei Fu, Wenan Zhang, and Bo Chen are with the College of Information Engineering, Zhejiang University of Technology, Hangzhou, 310023, China.

[2]Guangzhi Tian and Ling Shi are with the Department of Electronic and Computer Engineering, Hong Kong University of Science and Technology, Hong Kong, China.

Minglei Fu is the corresponding author, and the phone: +86-571-85292552; fax: 86-571-85292552; e-mail: fuml@zjut.edu.cn.

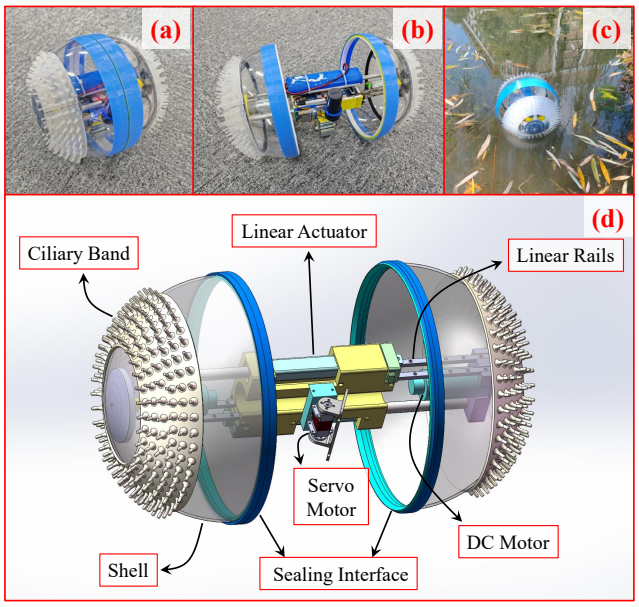

Fig. 1. Illustration of MorphoBall's design and system architecture. (a) Sealed spherical mode for robust traversal in dusty or rainy environments. (b) Deployed differential-drive mode enabling precise navigation and zero-radius turning on flat terrain. (c) Surface-swimming mode propelled by biomimetic ciliary bands. (d) MorphoBall complete robot design and details..

The remainder of this paper is organized as follows: Section II introduces the design and mechanism of MorphoBall. Section III derives its dynamic models, and Section IV presents the hierarchical control architecture. Section V evaluates performance through experiments, and Section VI concludes with key findings and future directions.

II. Robot Design and Mechanism

MorphoBall is designed for adaptive locomotion across diverse environments, morphing among three distinct modes: (1) a sealed spherical robot for robust terrain traversal; (2) a differential-drive wheeled vehicle for precise navigation; and (3) a surface-swimming platform propelled by biomimetic ciliary actuation.

The dual terrestrial modes are inspired by the armadillo's adaptive behavior [22]: while it typically relies on precise and agile crawling for efficient locomotion, it transitions into a defensive rolling posture to protect its vital organs when threatened or exposed to harsh environments. Similarly, our robot integrates two complementary modes of operation. The spherical form provides superior environmental sealing and post-impact stability, but its centroid-of-mass-based rolling suffers from limited mobility and dynamic instability on uneven terrain. To bridge this gap, we incorporate a deployable differential-drive system that ensures high-precision, stable locomotion under nominal conditions, while retaining the ability to morph into a fully sealed sphere for operation in rain, dust, or collision-prone scenarios. The following subsections detail the mechanical realization of this vision.

A. Seal-Integrated Morphing Shell Mechanism

The morphing shell of MorphoBall is centered around a rigid core platform, to which two symmetric actuation modules are mounted. Each module consists of a miniature linear actuator (stroke: 75 mm, force: 20 N) guided by a pair of parallel linear rails, ensuring precise and synchronized translational motion. At the distal end of each actuator, a DC motor (rated torque: 0.3 N·m) is rigidly coupled to one hemispherical shell, enabling independent rotational actuation of each half-shell relative to the core platform, essential for differential-drive locomotion. The opening and closing of the hemispheres are driven by coordinated extension/retraction of the linear actuators, under closed-loop position control using built-in quadrature encoders. This architecture ensures symmetric motion of both hemispheres with positional repeatability better than ± 0.5 mm. Furthermore, the inter-hemisphere spacing is dynamically adjustable via actuator stroke control, allowing real-time tuning of the wheelbase in differential-drive mode — a feature critical for adapting to varying terrain constraints.

As shown in Fig. 2, the sealing is achieved through a custom-designed dual-component sealing interface, comprising a male and female sealing ring pair mounted along the equatorial mating edges of the two hemispheres. The male ring features a V-shaped protrusion, while the female ring contains a complementary V-shaped recess, enabling passive mechanical alignment during closure and preventing lateral misalignment. Structurally, the sealing rings are composed of a dual-material system: the inner structural layer is fabricated from rigid ABS (Shore D 85) to maintain shell geometry and resist deformation under load; the outer contact layer is made of flexible TPU (Shore A 80) to enhance ground traction and provide impact damping during terrestrial rolling. The primary sealing functionality is provided by a thin, adhesive-bonded liner of thermoplastic rubber (TPR) embedded within the V-groove of the female ring. The TPR compound is plasticized with naphthenic oil to achieve an ultra-soft surface (Shore A < 15) with slight tackiness. Upon shell closure, this compliant layer conforms intimately to the male V-protrusion under minimal contact pressure, which is generated solely by the static friction of the linear actuators in their retracted state. This arrangement creates an airtight and watertight seal without requiring external clamping mechanisms or continuous power consumption[1].

B. Pendulum-Based CoM Shifter and Drive Device

In spherical rolling mode, CoM shifting is achieved through a pendulum arm mounted to the core platform via a hollow-core servo motor. This servo enables $\pm 90^\circ$ lateral oscillation of the pendulum relative to the platform, primarily for roll-axis stabilization and minor directional corrections. For primary locomotion, the robot synchronously drives two DC motors, enabling the core platform to rotate relative to the

[1]Notably, MorphoBall is designed primarily for surface swimming rather than deep submersion. During aquatic navigation, external water pressure passively compresses the TPR sealing liner, further enhancing watertightness without the need for deep-sea rated mechanisms.

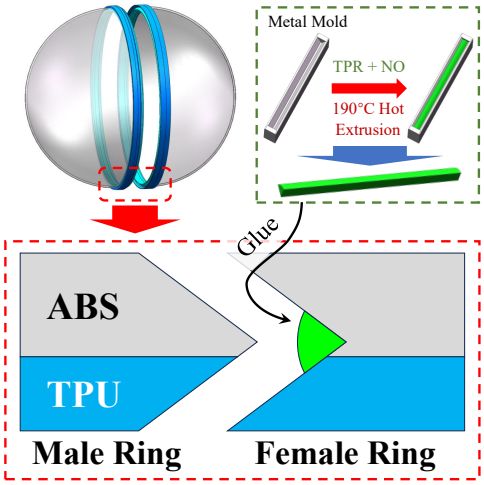

Fig. 2. Close-up of V-groove sealing interface (ABS structural layer, TPU contact layer, TPR sealing liner).

spherical shell. This co-rotation induces a controlled fore-aft CoM displacement, propelling the robot forward or backward via gravitational torque.

In differential-drive mode, the two hemispherical shells themselves serve as the primary drive wheels, eliminating the need for deployable appendages and preserving structural simplicity. The outer TPU layer of the sealing rings provides sufficient friction against typical terrestrial surfaces. Forward/backward motion is generated by co-rotating both shells in the same direction thereby shifting the system's CoM fore or aft to induce rolling (identical to the spherical mode). Steering is achieved by the differential rotation of the two shells.

C. Bionic Ciliary Band for Propulsion

The surface of MorphoBall's hemispherical shells is partially coated with biomimetic ciliary structures, fabricated by casting Shore A 30 silicone rubber into 3D-printed molds. Critically, uniform coverage of the entire shell would compromise terrestrial rolling dynamics and complicate kinematic modeling. To avoid this, we adopt a *functionally zoned design*, in which silicone micro-pillars are selectively applied within the 30°–60° latitudinal band on each hemisphere. This placement provides two distinct mechanical advantages depending on the operating environment.

During terrestrial rolling, the smooth equatorial contact zone ($\pm 30°$) ensures the robot maintains predictable motion. If the robot tilts excessively, the micro-pillar bands located beyond this $\pm 30°$ region passively contact the ground. This avoids the situation where lateral oscillations are difficult to alleviate through active control alone when the tilt angle is too large[2].

On water, the rotating micro-pillar bands sweep through the air-water interface, functioning as distributed paddles. During straight-line propulsion, symmetric immersion of both bands generates balanced hydrodynamic thrust. Steering is achieved by actively tilting the robot laterally to induce asymmetric waterline contact — only the lower hemisphere's band fully engages the water surface, generating a net yaw torque that turns the robot. This eliminates the need for dedicated rudders or additional actuators.

[2]Due to limited lateral centroid displacement authority, high-angle roll disturbances cannot be fully compensated algorithmically.

TABLE I

SPECIFIC PARAMETERS OF THE SIMULATION ENVIRONMENT.

R	radius of the sphere
m_{hb}	mass of a hemispherical shell
i_{hb}	moment of inertia of the hemispherical shell
m_p	mass of the pendulum
i_p	moment of inertia of the pendulum
l_p	distance between center of the sphere and CoM of the pendulum
m_c	mass of the core platform
i_c	moment of inertia of the core platform. i_c^p, i_c^r, and i_c^y represent the moments of inertia of the core platform about the pitch, roll, and yaw axes, respectively.
d	distance between the two hemispherical shells (when spherical, $d = 0$)
d_C	distance between the CoM of the two hemispherical shells
θ	rotation angle of the spherical shell
ϕ	rotational angle of the pendulum relative to the direction of gravity
ψ	robot's rotation angle (yaw angle)
τ_m	output torque of a single DC motor
τ_p	output torque of a servo motor

III. MODELING

Given that MorphoBall operates in three distinct morphological configurations, its locomotion dynamics are strategically decoupled into three canonical motion primitives to facilitate tractable control synthesis. Importantly, this decomposition is based on *motion behavior*, not morphological state: (i) rolling (common to both spherical and differential-drive modes), (ii) yaw spinning (exclusive to differential-drive mode), and (iii) surface swimming (aquatic mode). Corresponding nomenclature and parameters are defined in **Table I**.

A. Rolling Dynamics Model

As illustrated in Fig. 3 (a), the forward rolling motion in spherical mode, lateral tilting, and forward motion in differential-drive mode are all abstracted as a planar dynamical system consisting of a single-degree-of-freedom pendulum confined within a circular rim. Notably, the forward rolling dynamics in spherical mode and differential-drive mode share identical model parameters. Let M_b, M_p, I_b, and I_p denote the equivalent mass and moment of inertia of the shell and pendulum, respectively, in the rolling dynamics model; l represents the effective pendulum arm length, and τ is the torque applied to the pendulum joint. The parameter definitions differ between the two rolling behaviors as follows:

Forward Rolling: $M_b = 2m_{hb}$, $M_p = m_p + m_c$, $I_b = 2I_{hb}$, $I_p = i_c^p + i_p$, $l = l_p m_p/(m_c + m_p)$, $\tau = 2\tau_m$.

Tilting Rolling: $M_b = 2m_{hb}+m_c$, $M_p = m_p$, $I_b = 2i_{hb}+i_c^r$, $I_p = i_p$, $l = l_p$, $\tau = \tau_p$.

The kinetic energy of the spherical shell, T_b, is the sum of its translational and rotational components:

$$T_b = \frac{1}{2} M_b R^2 \dot{\theta}^2 + \frac{1}{2} I_b \dot{\theta}^2 = \frac{1}{2}(M_b R^2 + I_b)\dot{\theta}^2. \quad (1)$$

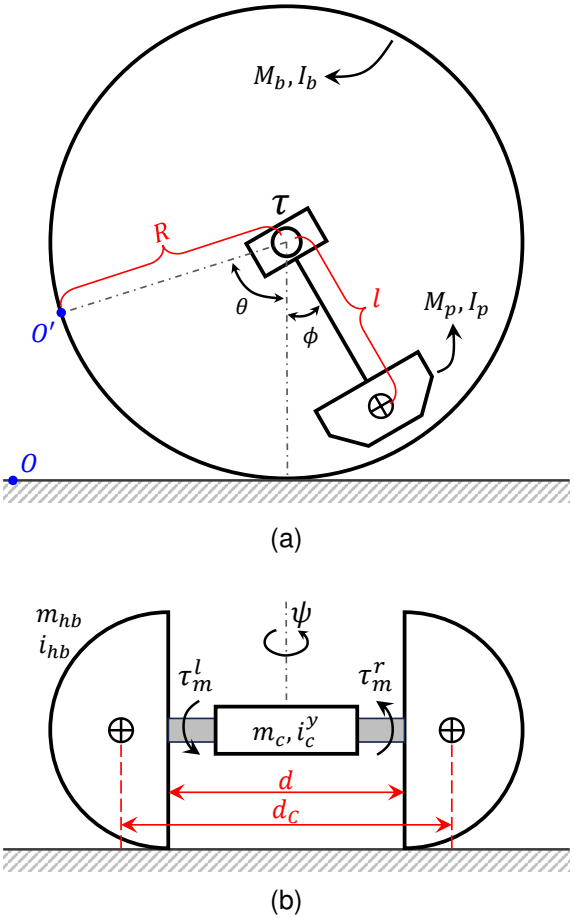

Fig. 3. Illustration of the dynamics model of MorphoBall. (a) Rolling dynamics model. (b) Differential rotation model.

The velocity of the pendulum's center of mass, $\mathbf{v}_p$, results from the superposition of the shell's translational velocity and the pendulum's relative motion in the shell-fixed frame. Its squared magnitude is:

$$\begin{aligned} v_p^2 &= (R\dot{\theta} + l\dot{\phi}\cos\phi)^2 + (l\dot{\phi}\sin\phi)^2 \\ &= R^2\dot{\theta}^2 + 2Rl\dot{\theta}\dot{\phi}\cos\phi + l^2\dot{\phi}^2(\cos^2\phi + \sin^2\phi) \\ &= R^2\dot{\theta}^2 + 2Rl\dot{\theta}\dot{\phi}\cos\phi + l^2\dot{\phi}^2. \end{aligned} \tag{2}$$

Thus, the kinetic energy of the pendulum, T_p, is:

$$\begin{aligned} T_p &= \frac{1}{2}M_p v_p^2 + \frac{1}{2}I_p\dot{\phi}^2 \\ &= \frac{1}{2}M_p(R^2\dot{\theta}^2 + 2Rl\dot{\theta}\dot{\phi}\cos\phi + l^2\dot{\phi}^2) + \frac{1}{2}I_p\dot{\phi}^2. \end{aligned} \tag{3}$$

Assuming the ground is flat, the system's potential energy after neglecting constant terms is:

$$V = -M_p g l\cos\phi. \tag{4}$$

The Lagrangian of the rolling system is constructed as $L = T_b + T_p + V$. Applying the Euler-Lagrange equation for each generalized coordinate q_i:

$$\frac{d}{dt}\left(\frac{\partial L}{\partial \dot{q}_i}\right) - \frac{\partial L}{\partial q_i} = Q_i, \tag{5}$$

where Q_i denotes the generalized force associated with coordinate q_i. For the rolling angle θ, no external force performs direct work under the no-slip assumption; hence, $Q_\theta = 0$. For the pendulum angle ϕ, the generalized force Q_ϕ corresponds to the actuation torque τ applied at the pivot. Substituting the energy expressions (1), (3), and (4) into (5), the equation of motion for θ becomes:

$$(MR^2 + I_b)\ddot{\theta} + (M_p Rl\cos\phi)\ddot{\phi} - (M_p Rl\sin\phi)\dot{\phi}^2 = 0, \tag{6}$$

where $M = M_b + M_p$ is the total system mass. The equation of motion for ϕ is:

$$(M_p l^2 + I_p)\ddot{\phi} + (M_p Rl\cos\phi)\ddot{\theta} + M_p gl\sin\phi = \tau. \tag{7}$$

Rearranging (6) and (7) into matrix form yields the coupled nonlinear dynamics:

$$\begin{bmatrix} MR^2 + I_b & M_p Rl\cos\phi \\ M_p Rl\cos\phi & M_p l^2 + I_p \end{bmatrix} \begin{bmatrix} \ddot{\theta} \\ \ddot{\phi} \end{bmatrix} = \begin{bmatrix} M_p Rl\sin\phi\,\dot{\phi}^2 \\ \tau - M_p gl\sin\phi \end{bmatrix}. \tag{8}$$

B. Differential Rotation Model

As shown in Fig. 3 (b), the rotational motion of MorphoBall in differential-drive mode is modeled as a planar two-wheel differential system. When considering only the yaw motion, the left and right wheels share one degree of freedom (i.e., the difference in rotational speed), rotating with the same magnitude but in opposite directions. The kinetic energy of the central platform is:

$$T_c = \frac{1}{2}i_c^y\dot{\psi}^2. \tag{9}$$

The kinetic energy of each wheel is:

$$T_w^l = T_w^r = \frac{1}{2}m_{hb}\left(\frac{d_C}{2}\dot{\psi}\right)^2 + \frac{1}{2}i_{hb}\left(\frac{\dot{\psi}d}{2R}\right)^2. \tag{10}$$

The total kinetic energy (Lagrangian, as potential energy is constant) is:

$$\begin{aligned} L = T &= T_c + T_w^l + T_w^r \\ &= \frac{1}{2}i_c^y\dot{\psi}^2 + m_{hb}\left(\frac{d_C}{2}\dot{\psi}\right)^2 + i_{hb}\left(\frac{\dot{\psi}d}{2R}\right)^2 \\ &= \frac{1}{2}\left[i_c^y + 2m_{hb}\left(\frac{d_C}{2}\right)^2 + i_{hb}\left(\frac{d}{2R}\right)^2\right]\dot{\psi}^2 \\ &= \frac{1}{2}I_{eff}\dot{\psi}^2, \end{aligned} \tag{11}$$

where the effective moment of inertia about the yaw axis is defined as:

$$I_{eff} = i_c^y + \frac{1}{2}m_{hb}{d_C}^2 + \frac{1}{2}i_{hb}\left(\frac{d}{R}\right)^2. \tag{12}$$

Applying the Euler-Lagrange equation with generalized force $Q_\psi = \frac{d}{2R}(d\tau_m^r - d\tau_m^l)$ (the differential torque input), the equation of motion simplifies to:

$$I_{eff}\ddot{\psi} = \frac{d}{2R}(d\tau_m^r - d\tau_m^l). \tag{13}$$

C. Surface Swimming Model

MorphoBall's locomotion on water is primarily driven by viscous drag forces acting on the ciliary bands during shell rotation[3]. However, due to the highly complex fluid-structure interaction, an accurate full hydrodynamic model is infeasible. We therefore simplify the dynamics into two decoupled components: forward motion and yaw motion. The control inputs are assumed to be the shell's forward rolling angular velocity $\dot{\theta}_p$ and the robot's roll tilt angle θ_r.

The propulsive force F_{thrust} is modeled as proportional to $\dot{\theta}_p$ and modulated by $\cos\theta_r$, which captures the effective radius of ciliary engagement:

$$F_{thrust} = k_t \dot{\theta}_p \cos\theta_r, \tag{14}$$

where k_t is the thrust coefficient (N·s/rad). The yaw torque τ_{yaw} arises from the horizontal rotational component of the ciliary paddling motion beneath the waterline. Its magnitude is proportional to both $\dot{\theta}_p$ and $\sin\theta_r$.

$$\tau_{yaw} = k_m \dot{\theta}_p \sin\theta_r, \tag{15}$$

where k_m is the yaw torque coefficient (N·m·s/rad). Hydrodynamic drag force F_{drag} and yaw drag torque τ_{drag} are modeled linearly with respect to velocity:

$$F_{drag} = -c_d v \text{ and } \tau_{drag} = -c_w \dot{\psi}, \tag{16}$$

where v is the forward velocity, c_d is the drag coefficient (N·s/m), and c_w is the yaw drag coefficient (N·m·s/rad). The forward and yaw dynamics are then:

$$\begin{aligned} &(2m_{hb} + m_c + m_p)\,\dot{v} = F_{thrust} + F_{drag}, \\ &\iff \dot{v} = \frac{k_t \dot{\theta}_p \cos\theta_r - c_d v}{2m_{hb} + m_c + m_p}, \end{aligned} \tag{17}$$

$$\begin{aligned} &\left(i_c^y \cos^2\theta_r + i_c^r \sin^2\theta_r + 2i_{hb}\right)\ddot{\psi} = \tau_{yaw} + \tau_{drag}, \\ &\iff \ddot{\psi} = \frac{k_m \dot{\theta}_p \sin\theta_r - c_w \dot{\psi}}{i_c^y \cos^2\theta_r + i_c^r \sin^2\theta_r + 2i_{hb}}. \end{aligned} \tag{18}$$

To simplify the model, we assume that the moment of inertia of the core platform is uniform under this mode, i_c, therefore (18) can be simplified as:

$$\ddot{\psi} = \frac{k_m \dot{\theta}_p \sin\theta_r - c_w \dot{\psi}}{i_c + 2i_{hb}}. \tag{19}$$

Due to the complexity of fluid-structure interactions, the hydrodynamic and thrust coefficients (c_d, c_w, k_t, k_m) in this paper are empirically estimated through steady-state experimental measurements of physical prototypes.

[3]At low relative velocities between cilia and water (typically < 0.2 m/s in our experiments), the system operates in a low Reynolds number regime where viscous drag dominates over pressure drag, thus scaling linearly with relative speed.

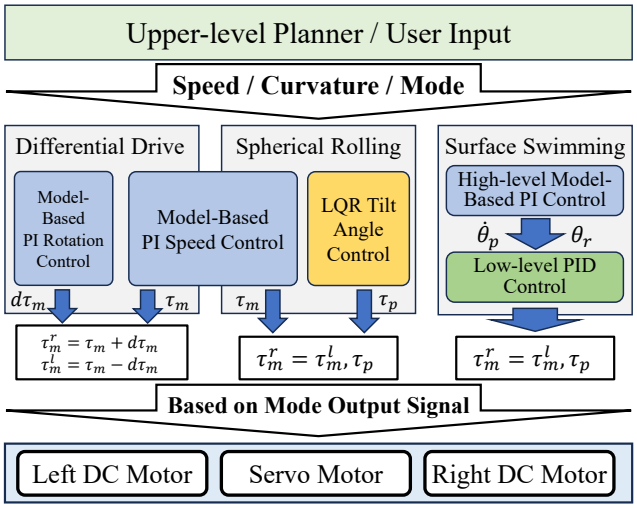

Fig. 4. Illustration of MorphoBall's control architecture.

IV. Motion Control

The control architecture of MorphoBall is illustrated in Fig. 4. MorphoBall switches locomotion modes based on commands from a high-level planner or user input. The controller takes the desired forward velocity v and trajectory curvature κ (determined by tilt angle or differential speed) as control targets, and generates actuator commands accordingly. The control system consists of three sub-controllers: a model-based PI controller, an LQR controller, and a PID controller. Notably, the forward motion in both differential-drive mode and spherical rolling mode shares the same model-based PI controller. The tilt-angle control in spherical rolling mode and surface swimming mode shares the same LQR controller. The implementation of each controller under its respective mode is detailed in the following subsections.

A. Spherical Rolling Control

For spherical rolling control, we design two distinct controllers to regulate the robot's forward velocity v and trajectory curvature κ, respectively. Both utilize the same dynamics derived in Subsection III.A, but target different control objectives.

Trajectory curvature control is achieved by regulating the shell's roll tilt angle θ_r to a desired setpoint. The relationship between θ_r and κ is approximated as:

$$\kappa = \frac{R}{\tan\theta_r}. \tag{20}$$

For θ_r control of the system described by (8), LQR has been widely adopted in prior work for similar underactuated systems. Assuming the system is stabilized at $\theta_r = \theta_r^g$ with $\dot{\theta}_r = \dot{\phi} = 0$, we linearize (8) around this equilibrium and neglect higher-order terms to obtain:

$$\begin{bmatrix} MR^2 + I_b & M_p Rl \\ M_p Rl & M_p l^2 + I_p \end{bmatrix} \begin{bmatrix} \ddot{\theta} \\ \ddot{\phi} \end{bmatrix} = \begin{bmatrix} 0 \\ \tau - M_p g l \phi \end{bmatrix}. \tag{21}$$

Let $\mathbf{x} = [\theta_r - \theta_r^g, \phi, \dot{\theta}_r, \dot{\phi}]^T$. Equation (21) is then expressed in standard state-space form $\dot{\mathbf{x}} = A\mathbf{x} + B\tau$. The optimal

control law is obtained by minimizing the cost function:

$$J = \int_0^\infty (\mathbf{x}^T Q \mathbf{x} + \tau R \tau)\, dt, \tag{22}$$

with weighting matrices selected through iterative experimentation and tuning as $Q = \text{diag}(800, 1, 15, 1)$, $R = 4$. The resulting feedback gain K_κ is computed offline and stored for real-time execution:

$$\tau = -K_\kappa \mathbf{x}. \tag{23}$$

For velocity control, we regulate the shell's forward rolling angular velocity $\dot{\theta}_p$ to achieve the desired body velocity. The kinematic relationship is:

$$v = \dot{\theta}_p R \cos\theta_r. \tag{24}$$

Substituting $\ddot{\phi}$ from (7) into (6), and rearranging, yields the feedforward+feedback torque command:

$$\begin{aligned} 2\tau_m = &\left(M_p R l \dot{\phi}^2 \sin\phi - (MR^2 + I_b)\ddot{\theta}_p\right) \frac{M_p l^2 + I_p}{M_p R l \cos\phi} \\ &+ (M_p R l \cos\phi)\ddot{\theta}_p + M_p g l \sin\phi. \end{aligned} \tag{25}$$

Substituting (26) for $\ddot{\theta}_p$, we obtain the robot velocity control law:

$$\ddot{\theta}_p = \cos\theta_r \left(K_v^p \left(\tfrac{v^g}{R\cos\theta_r} - \dot{\theta}_p\right) + K_v^i \textstyle\int \tfrac{v^g}{R\cos\theta_r} - \dot{\theta}_p\, dt\right). \tag{26}$$

B. Differential Drive Control

In differential-drive mode, forward velocity control is achieved by setting $\theta_r = 0$ in (26). The relationship between trajectory curvature and yaw rate is $\dot{\psi} = \kappa v$. Using (13), the model-based PI controller for curvature tracking is:

$$\tau_m^r = -\tau_m^l = \frac{I_{eff} R}{d} \ddot{\psi}, \tag{27}$$

where $\ddot{\psi}$ is designed as:

$$\ddot{\psi} = K_\kappa^p \left(\kappa^g v - \dot{\psi}\right) + K_\kappa^i \int \kappa^g v - \dot{\psi}\, dt. \tag{28}$$

C. Surface Swimming Control

In surface swimming mode, the controller is structured in two layers. The high-level controller generates the reference forward rolling angular velocity $\dot{\theta}_p$ and roll tilt angle θ_r required to track the desired speed and curvature. These references are then passed to the low-level controller, which outputs the final actuator commands. The low-level controller is implemented as a PID regulator to simplify design and ensure fast response.

The high-level controller is designed as a model-based PI controller using the surface swimming dynamics in (17) and (18). Specifically, the controller for forward velocity v is:

$$\dot{\theta}_p = \frac{(2m_{hb} + m_c + m_p)\,\dot{v} + c_d v}{k_t \cos\theta_r}, \tag{29}$$

where $\dot{v}$ is replaced by:

$$\dot{v} = K_{s,v}^p (v^g - v) + K_{s,v}^i \int v^g - v\, dt. \tag{30}$$

The controller for trajectory curvature κ is:

$$\theta_r = \arcsin\left(\frac{(i_c + 2i_{hb})\,\ddot{\psi} + c_w \dot{\psi}}{k_m \dot{\theta}_p}\right), \tag{31}$$

where $\ddot{\psi}$ is replaced by:

$$\ddot{\psi} = K_{s,\kappa}^p \left(\kappa^g v - \dot{\psi}\right) + K_{s,\kappa}^i \int \kappa^g v - \dot{\psi}\, dt. \tag{32}$$

V. Experimental Evaluation

To validate the effectiveness of MorphoBall's morphological design and control architecture, we conduct a tiered experimental evaluation: (i) low-level motion control performance, (ii) aquatic propulsion comparison, (iii) indoor navigation under structured constraints, and (iv) outdoor multi-terrain traversal with mode switching. All experiments are conducted on the physical prototype, with quantitative metrics captured via onboard sensors and external motion capture (OptiTrack).

A. Motion Control Performance

We evaluate the stability and dynamic response of our model-based controllers against a baseline PID implementation, focusing on two critical behaviors:

(i) Forward Velocity Tracking in Differential-Drive Mode. The robot is commanded to track a step velocity profile: accelerate to $v^g \in \{0.1, 0.3, 0.5\}$ m/s for 5 seconds, then decelerate to 0 m/s. As shown in Fig. 5 (a), the model-based PI controller achieves smooth acceleration/deceleration, and the pitch oscillation is smaller. In contrast, the PID baseline exhibits significant pitch overshoot and velocity jitter during transients (for larger v^g this is obvious), demonstrating the advantage of feedforward compensation and inertia-aware control.

(ii) Roll Tilt Regulation in Spherical Mode. The robot is commanded to switch its roll tilt angle θ_r between $+20^\circ$ and -20° every 4 seconds. Fig. 5 (b) shows that the LQR controller achieves stable, damped transitions with settling time < 1.5 s and overshoot $< 13\%$. The PID controller lacking dynamic coupling compensation exhibits continuous oscillation and takes longer to stabilize.

B. Aquatic Propulsion Comparison

To evaluate the impact of the ciliary band on MorphoBall's aquatic performance, we conduct a comparative study in a static water pool, measuring both short-distance acceleration and rotational maneuverability.

For the acceleration test, the robot starts from rest with $\theta_r = 0^\circ$ and is driven at a constant rolling angular velocity of $\dot{\theta}_p = 1.57$ rad/s. The time required to travel 0.5 m is recorded, ensuring that the motion remains within the acceleration phase. For the turning test, the robot starts from rest with $\theta_r = 60^\circ$ and is driven at the same rolling angular velocity ($\dot{\theta}_p = 1.57$ rad/s). The time required to complete a 4π rotation is recorded.

The results, averaged over five trials, demonstrate significant improvements with the ciliary band. For acceleration, the average time to travel 0.5 m is 5.37 s with the ciliary

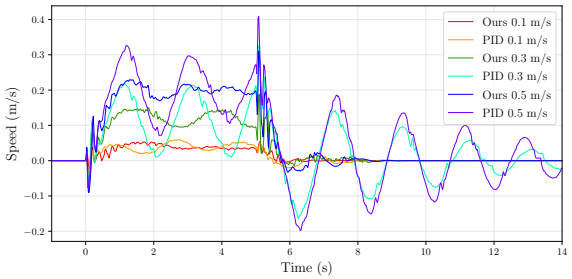

(a)

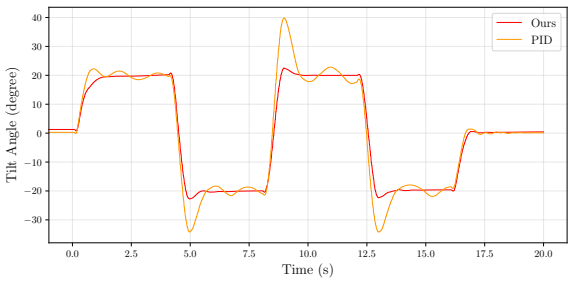

(b)

Fig. 5. Illustration of motion control performance. (a) Forward velocity response. (b) Roll tilt angle tracking.

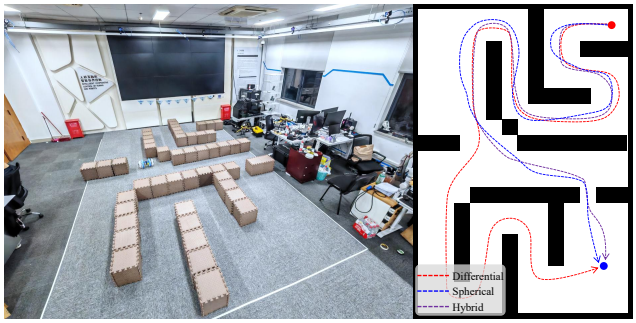

Fig. 6. Indoor navigation schematic. The left side shows the indoor experimental environment, and the right side displays the robot's movement trajectories under three strategies.

TABLE II

INDOOR NAVIGATION PERFORMANCE (N=5 TRIALS)

Strategy	Navigation Success Rate	AVG. Time (s)	AVG. Movement Distance (m)
Spherical-Only	60%	62.7	13.67
Differential-Only	100%	50.8	17.41
Hybrid Morphing	100%	41.3	13.05

band, compared to 11.26 s without it. For turning, the average time to complete a 4π rad rotation is 13.23 s with the ciliary band, compared to 16.98 s without it. These findings highlight the dual-function ciliary band's critical role in enhancing both thrust generation and steering agility during aquatic navigation.

C. Indoor Navigation

We evaluate navigation efficiency in a structured indoor environment (4 m $\times$ 9 m) with a narrow slit 30 cm wide that can only be traversed in spherical mode, and winding corridors that favor differential-drive agility. We compare three navigation strategies: Spherical-Only, Differential-Drive-Only, and Hybrid Morphing.

Path planning is implemented using A* over a Probabilistic Roadmap (PRM). For the hybrid mode, separate PRMs are maintained for each morphology, and transitions between modes incur a cost equivalent to two seconds of travel time. Trajectory tracking is implemented using the DWA algorithm, and robot localization is provided by the OptiTrack system.

As shown in Table II, the hybrid morphing strategy reduces total travel time by 34% compared to the spherical-only mode while successfully navigating the narrow slit. In contrast, the differential-drive-only strategy is forced into a significantly longer detour, increasing path length by 4.4 m and travel time by 23%. The 40% failure rate in the spherical-only mode was primarily due to severe collisions with environmental obstacles. Pure spherical rolling inherently suffers from limited control authority and underactuation, making precise dynamic obstacle avoidance challenging during DWA trajectory tracking Fig. 6 illustrates the trajectories executed under each strategy and highlights the efficiency gain enabled by morphology adaptation.

D. Outdoor Multi-terrain Tracing

We conduct a comprehensive outdoor test on a 127-meter course traversing dry pavement, a simulated rain zone (sprinklers), a grass field, and a shallow pond. The global path is precomputed from prior terrain mapping; the robot positioning uses RTK-GPS with an accuracy of ±1 cm. Mode transitions are triggered autonomously based on real-time terrain classification: the robot switches to differential-drive on hard surfaces, to spherical mode in wet or vegetated areas for sealing and obstacle resilience, and to surface swimming upon detecting water.

The MorphoBall satellite trajectory recorded in the experiment is shown in the Fig. 7. During this process, MorphoBall successfully traverses all terrains, executing 4 seamless mode transitions. Total mission time averaged 352 seconds. Video footage confirms stable swimming propulsion and effective roll damping on slopes. This experiment conclusively demonstrates MorphoBall's superior environmental adaptability through morphological reconfiguration.

VI. CONCLUSION

This paper demonstrates that morphological reconfiguration can serve as an active strategy to optimize robotic mobility across heterogeneous environments. The integration of dual-mode terrestrial locomotion and surface swimming into a unified platform not only expands operational versatility but also enables intelligent path planning based on terrain constraints. The dual-function ciliary band exemplifies a design philosophy where passive structural features synergize with active control systems, offering a blueprint

Fig. 7. Illustration of outdoor multi-terrain tracing. The movement track recorded by RTK-GPS on the right.

for future soft robotic systems. Potential applications include search-and-rescue operations in disaster zones, environmental monitoring in wetlands, and autonomous exploration in mixed indoor-outdoor settings. Future work will focus on enhancing energy efficiency through optimized actuation, integrating onboard perception for fully autonomous operation, and exploring cooperative behaviors in multi-robot systems. These advancements could further bridge the gap between theoretical designs and real-world deployments of adaptive mobile robots.

APPENDIX

To facilitate reproducibility and further research, we have made the design files and source code for MorphoBall publicly available in a repository hosted on GitHub: `https://github.com/TZY-H/SphericalRobot_Transforms-.git`.

A supplementary video demonstration of this work is publicly accessible online at: `https://youtu.be/gKpjVtqAP_I`.

REFERENCES

[1] Y. Wan, Y. Zhong, A. Ma, and L. Zhang, "An accurate uav 3-d path planning method for disaster emergency response based on an improved multiobjective swarm intelligence algorithm," *IEEE Transactions on Cybernetics*, vol. 53, no. 4, pp. 2658–2671, 2022.

[2] V. M. Baez, "Drone measurements of wetland soils & robotic manipulation of ensembles using global forces," Master's thesis, University of Houston, 2021.

[3] M. Spenko, "Making contact: A review of robotic attachment mechanisms for extraterrestrial applications," *Advanced Intelligent Systems*, vol. 5, no. 3, p. 2100063, 2023.

[4] M. Taheri Andani, Z. Ramezani, S. Moazami, J. Cao, M. M. Arefi, and H. Zargarzadeh, "Observer-based sliding mode control for path tracking of a spherical robot," *Complexity*, vol. 2018, no. 1, p. 3129398, 2018.

[5] S. A. Tafrishi, M. Svinin, E. Esmaeilzadeh, and M. Yamamoto, "Design, modeling, and motion analysis of a novel fluid actuated spherical rolling robot," *Journal of Mechanisms and Robotics*, vol. 11, no. 4, p. 041010, 2019.

[6] S.-B. Chen, A. Beigi, A. Yousefpour, F. Rajaee, H. Jahanshahi, S. Bekiros, R. A. Martínez, and Y. Chu, "Recurrent neural network-based robust nonsingular sliding mode control with input saturation for a non-holonomic spherical robot," *IEEE Access*, vol. 8, pp. 188 441–188 453, 2020.

[7] B. Belzile and D. St-Onge, "Design and modeling of a spherical robot actuated by a cylindrical drive," in *Proc. IEEE International Conference on Robotics and Automation (ICRA)*, 2022, pp. 1169–1175.

[8] J. Huo, R. Lin, and M. Yang, "Design and validation of a novel adaptive motion control for a pendulum spherical robot," *Robotica*, vol. 41, no. 7, pp. 2031–2049, 2023.

[9] Y. Liu, Y. Wang, X. Guan, Y. Wang, S. Jin, T. Hu, W. Ren, J. Hao, J. Zhang, and G. Li, "Multi-terrain velocity control of the spherical robot by online obtaining the uncertainties in the dynamics," *IEEE Robotics and Automation Letters*, vol. 7, no. 2, pp. 2732–2739, 2022.

[10] A. Nakashima, S. Maruo, R. Nagai, and N. Sakamoto, "2-dimensional dynamical modeling and control of spherical robot driven by inner car," in *Proc. IEEE International Conference on Robotics and Biomimetics (ROBIO)*, 2018, pp. 1846–1851.

[11] G. V. Belskii, E. V. Serykh, and D. A. Pankratev, "Design and implementations of spherical robot hardware level," in *Proc. IEEE Conference of Russian Young Researchers in Electrical and Electronic Engineering (ElConRus)*, 2021, pp. 806–809.

[12] M. Bujňák, R. Pirník, D. Nemec, J. Kafková, A. Janota, and P. Kuchár, "Spheridrive: A spherical robot with an innovative 3-wheeled platform and omnidirectional wheels," *Results in Engineering*, vol. 25, p. 104351, 2025.

[13] Q. Zhang, Y. Li, Y.-A. Yao, and R. Li, "Design and locomotivity analysis of a novel deformable two-wheel-like mobile mechanism," *Industrial Robot: the International Journal of Robotics Research and Application*, vol. 47, no. 3, pp. 369–380, 2020.

[14] M. Oevermann, D. Pravecek, G. Jibrail, R. Jangale, and R. O. Ambrose, "Roboball: An all-terrain spherical robot with a pressurized shell," in *Proc. IEEE International Conference on Robotics and Automation (ICRA)*, 2024, pp. 13 502–13 508.

[15] F. Wang, C. Li, S. Niu, P. Wang, H. Wu, and B. Li, "Design and analysis of a spherical robot with rolling and jumping modes for deep space exploration," *Machines*, vol. 10, no. 2, p. 126, 2022.

[16] S. Guo, S. Sun, and J. Guo, "Design of a sma-based salps-inspired underwater microrobot for a mother-son robotic system," in *Proc. IEEE International Conference on Mechatronics and Automation (ICMA)*, 2017, pp. 1314–1319.

[17] X. Ma, G. Wang, and K. Liu, "Design and optimization of a multimode amphibious robot with propeller-leg," *IEEE Transactions on Robotics*, vol. 38, no. 6, pp. 3807–3820, 2022.

[18] J. Yu, R. Ding, Q. Yang, M. Tan, W. Wang, and J. Zhang, "On a bio-inspired amphibious robot capable of multimodal motion," *IEEE/ASME Transactions on Mechatronics*, vol. 17, no. 5, pp. 847–856, 2011.

[19] S. Guo, Y. He, L. Shi, S. Pan, R. Xiao, K. Tang, and P. Guo, "Modeling and experimental evaluation of an improved amphibious robot with compact structure," *Robotics and Computer-Integrated Manufacturing*, vol. 51, pp. 37–52, 2018.

[20] S. Guo, S. Mao, L. Shi, and M. Li, "Design and kinematic analysis of an amphibious spherical robot," in *Proc. IEEE International Conference on Mechatronics and Automation*, 2012, pp. 2214–2219.

[21] W. Ren, Y. Wang, H. Liu, S. Jin, Y. Wang, Y. Liu, Z. Zhang, T. Hu, and G. Li, "Spherical robot: A novel robot for exploration in harsh unknown environments," *IET Cyber-Systems and Robotics*, vol. 5, no. 4, p. e12099, 2023.

[22] M. Superina and W. Loughry, "Life on the half-shell: consequences of a carapace in the evolution of armadillos (xenarthra: Cingulata)," *Journal of Mammalian evolution*, vol. 19, no. 3, pp. 217–224, 2012.